Distinct Signatures of Electron-Phonon Coupling Observed in the Lattice Thermal Conductivity of NbSe₃ Nanowires

Lin Yang, ^{1,†} Yi Tao, ^{2,†} Jinyu Liu, ³ Chenhan Liu, ² Qian Zhang, ¹ Manira Akter, ⁴ Yang Zhao, ¹

Terry T. Xu, ⁴ Yaqiong Xu, ^{5,6} Zhiqiang Mao, ^{3,7,*} Yunfei Chen, ^{2,*} and Deyu Li^{1,*}

²School of Mechanical Engineering and Jiangsu Key Laboratory for Design and Manufacture of Micro-Nano Biomedical Instruments, Southeast University, Nanjing, 210096, P. R. China.

³Department of Physics and Engineering Physics, Tulane University, New Orleans, LA 70118, USA.

⁴Department of Mechanical Engineering and Engineering Science, The University of North Carolina at Charlotte, Charlotte, NC 28223, USA.

⁵Department of Electrical Engineering and Computer Science, Vanderbilt University, Nashville, TN 37235, USA.

⁶Department of Physics and Astronomy, Vanderbilt University, Nashville, TN 37235, USA.

⁷Department of Physics, Pennsylvania State University, University Park, PA 16802.

†: These authors contributed equally to this work

*: Author to whom correspondence should be addressed

E-mails: <u>zmao@tulane.edu; yunfeichen@seu.edu.cn; deyu.li@vanderbilt.edu</u>

¹Department of Mechanical Engineering, Vanderbilt University, Nashville, TN 37235, USA.

Abstract: The last two decades have seen tremendous progress in quantitative understanding of several major phonon scattering mechanisms (phonon-phonon, phonon-boundary, phonon-defects), as they are the determinant factors in lattice thermal transport that is critical for the proper functioning of various electronic and energy conversion devices. However, the roles of another major scattering mechanism, electron-phonon (e-ph) interactions, remain elusive. This is largely due to the lack of solid experimental evidence for the effects of e-ph scattering in the lattice thermal conductivity for the material systems studied thus far. Here we show distinct signatures in the lattice thermal conductivity observed below the charge density wave transition temperatures in NbSe₃ nanowires, which cannot be recaptured without considering e-ph scattering. Our findings can serve as the cornerstone for quantitative understanding of the e-ph scattering effects on lattice thermal transport in many technologically important materials.

Keywords: electron-phonon coupling, lattice thermal conductivity, charge density waves, van der Waals crystals, quasi-one-dimensional materials

The interaction between electrons and phonons is a fundamental process in solids, and it plays critical roles in various physical phenomena, such as superconductivity, hot carrier transport, and charge density waves. Indeed, e-ph scattering is a major mechanism of electrical resistance; and the effects of e-ph interactions on electronic properties of condensed matters have been extensively studied. However, while it is widely speculated that e-ph scattering could also affect lattice thermal conductivity, its contribution is still in debate and quantitative analyses have been largely lacking until recently.

The major challenge in understanding how e-ph interactions contribute to thermal conductivity lies in the either electron- or phonon-dominant thermal transport. For normal metals with typical carrier concentrations greater than $10^{22}\,\mathrm{cm}^{-3}$, phonons contribute less than 10% to the total thermal conductivity at all temperatures. While for semiconductors and insulators, phonons are the predominant heat carriers, and the effect of e-ph scattering is often neglected. However, it has recently been suggested that in various technically important materials, e-ph interactions can significantly reduce lattice thermal conductivity, which are attracting attention to the quantitative analyses of the e-ph coupling effect. 8–14

Attempts have been made earlier to measure the thermal conductivity of heavily doped semiconductors and investigate the effects of e-ph coupling on lattice thermal conductivity; 9,10 however, due to the inherent complexity of phonon scattering process involving multiple scattering mechanisms, it is extremely challenging to distinguish the contribution of e-ph scattering from other scattering mechanisms, especially at elevated temperatures. As such, the analyses tend to be qualitative. More recently, using a three-pulse femtosecond photoacoustic technique, Liao et al. measured the scattering rate of the 250 GHz phonons in Si membrane to quantify the e-ph interactions on phonon transport. However, the study is restricted to monochromatic phonons

and it also remains unclear whether the dynamically pumped electron-hole pairs have the same phonon scattering rate as normal electrons. To avoid the challenge of experimentally extracting the effects of e-ph scattering, first-principles calculations have been conducted on metals and heavily doped semiconductors. Although recent predictions both pointed out the significance of e-ph scattering on lattice thermal conductivity in some metals, discrepancies do exist between calculations such as for a normal metal Al: while Wang et al. 2 suggested that e-ph interactions only led to marginal difference, Jain and McGaughey predicted that e-ph scattering could lead to ~20% drop to the Al lattice thermal conductivity. Moreover, Liao et al. 2 claimed that up to ~45% reduction of lattice thermal conductivity could be induced by e-ph scattering in heavily-doped silicon, which has been overlooked in most previous studies.

To reconcile these discrepancies, experimental evidence for the contribution of e-ph interactions to lattice thermal conductivity has to be obtained. However, without a distinct signature such as the T^{-l} temperature dependence for Umklapp scattering, it is extremely difficult to distinguish the effects of e-ph interactions from other factors such as defect scattering. In this paper, we report such distinct signatures of e-ph coupling in lattice thermal conductivity observed with niobium triselenide (NbSe₃) nanowires, which clearly demonstrates the importance of e-ph scattering in lattice thermal conductivity.

NbSe₃ belongs to a class of van der Waals (vdW) materials with quasi-one-dimensional (quasi-1D) crystal structures, where covalently-bonded molecular chains are assembled together *via* vdW force. Owing to the restricted dimensionality, the density of free electrons in NbSe₃ spontaneously develops a wave-like variation when temperature drops below a critical value (T_{CDW}), which is called charge density waves (CDWs).^{3,15,16} The variation of charge carrier

concentration upon the onset of CDW modulates the e-ph scattering strength, resulting in unique features in the lattice thermal conductivity.

The monoclinic room-temperature structure of NbSe₃ is depicted in Figure 1a. NbSe₃ contains three types of metallic chains (Figure 1b) according to the strength of the chalcogen-chalcogen bonds in the unit cell. The type-III chains are responsible for the first CDW below $T_{CDWI} = 145 \text{ K}$ and the type-I chains contribute to the second modulation below $T_{CDW2} = 59 \text{ K}$, whereas the type-II chains remain metallic at all temperatures.¹⁷ Therefore, NbSe₃ does not develop a complete gap at the Fermi level, but remains partially metallic at low temperature.¹⁷

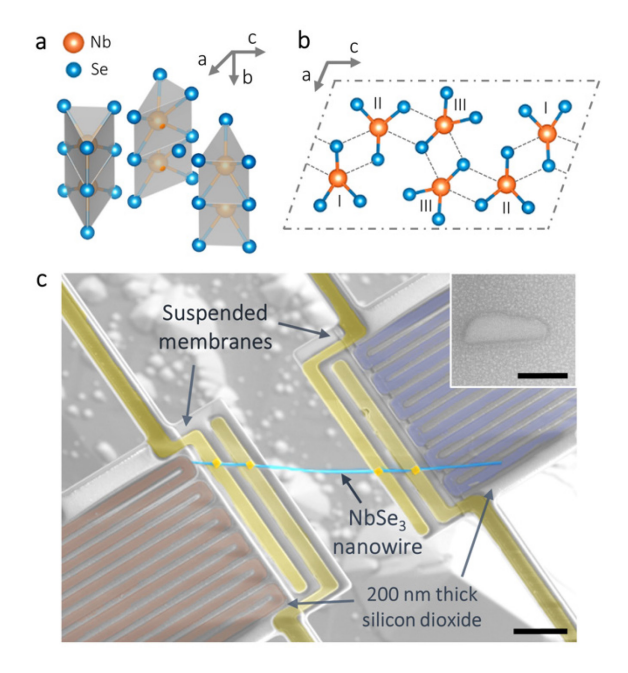


Figure 1. Crystal structure of NbSe3 and the suspended microdevice for thermal/electrical measurements. (a) Schematic diagram showing the stacking of the prisms along the *b* axis in NbSe3. (b) A projection of the crystal structure perpendicular to the *b* axis. (c) False-color SEM micrograph showing the measurement device with a NbSe3 nanowire. Pt/C was locally deposited *via* electron-beam induced deposition at the contacts between the nanowire and the four electrodes to enhance thermal/electrical contact. 200 nm thick silicon dioxide covers the Pt serpentine coils on both membranes. (Inset) An SEM image of the cross section of a NbSe3 nanowire. Scale bars: 4 μm (main panel); 100 nm (inset).

NbSe₃ nanowires were prepared from bulk crystals using ultrasonic cleaving, and even though the bonding energies along b- and c-directions in NbSe₃ are comparable, the Nb-Se bonds formed along c-direction vary significantly in the bond length (2.73 to 2.95 Å), which results in an easy cleavage. We measured the electrical and thermal conductivities, as well as Seebeck coefficients of the NbSe₃ nanowires using a well-established approach. As shown in Figure 1c, a nanowire is placed between two suspended SiN_x membranes with integrated Pt heaters/resistance thermometers and extra electrodes. For quasi-1D nanowires prepared via ultrasonic exfoliation, the cross-sections tend to be of irregular shapes, which we examine directly by cutting open the cross-section using focused ion beam (inset in Figure 1c). It has been shown that the hydraulic diameter (D_h), which is four times of the reciprocal of the surface-area-to-volume ratio (S/V), better characterizes the classical size effects in nanowires; 22,23 and here we use D_h to define the nanowire size.

Figure 2a shows the measured electrical resistance (R) of a NbSe₃ nanowire with $D_h = 135$ nm. During the electrical resistance measurement, to exclude the effects from CDW sliding, we set the electric field to be much smaller than the measured depinning threshold electric field of the NbSe₃ nanowire with the same cross-sectional area (Section III Supporting Information). At temperatures above 145 K, R decreases as the temperature reduces, indicating a metallic behavior. However, two evident anomalies are observed at 145 K and 59 K, where R increases abruptly and reaches maxima at 130 K and 43 K, respectively. The amplitudes of the two peaks are 11% (T_{CDWI}) and 30% (T_{CDW2}) of the room temperature resistance, in good agreement with those reported for bulk NbSe₃. ¹⁸

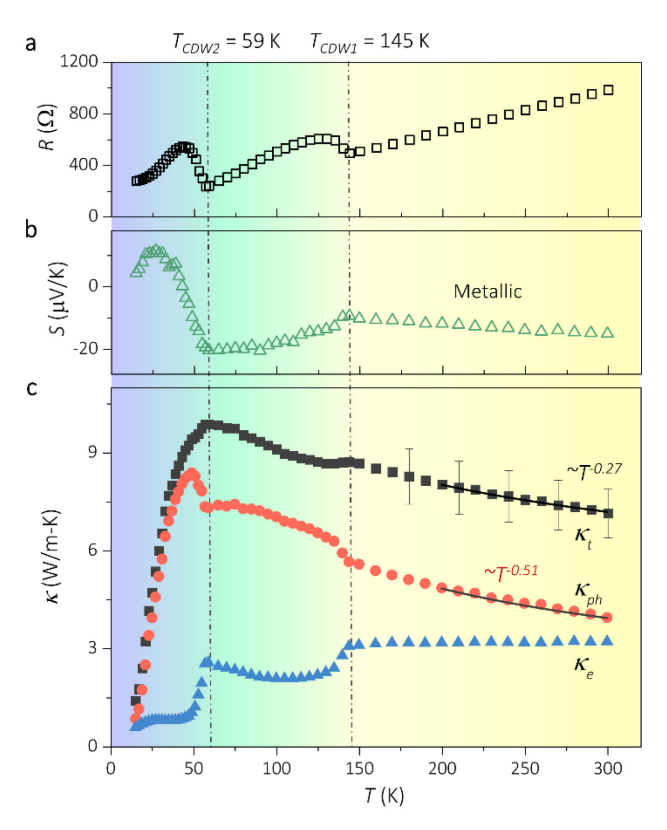


Figure 2. Distinct signatures of e-ph scattering in lattice thermal conductivity due to charge density waves. Measured electrical resistance (a), Seebeck coefficient (b), and thermal conductivity (c) of a 135 nm-diameter NbSe₃ nanowire in the temperature range of 15-300 K. The suspended length is 8.8 μ m. The charge density wave (CDW) phase transition points at 145 K and 59 K have been identified from the measured data. The error bars for selected data points of κ_t are shown in (c). The magnitude of the error bars are smaller than the symbol size for the electrical resistance and Seebeck coefficient, and are not included in (a-b).

Figure 2b displays the Seebeck coefficient, which is similar to that of bulk NbSe₃.²⁵ Importantly, following the parabolic energy band assumption, the Lorenz number, L, can be derived via solutions to the Boltzmann transport equation based on the measured Seebeck coefficient,²⁶ which allows for calculation of the electron contribution to thermal conductivity using the Wiedemann-Franz (WF) law. The maximum deviation of the extracted L from the degenerate limit, $L_0 = 2.44 \times 10^{-8} \text{ W}\Omega\text{K}^{-2}$, occurs at 59 K with a value of $2.4 \times 10^{-8} \text{ W}\Omega\text{K}^{-2}$, only ~1.6% lower than L_0 . Therefore, it is reasonable to adopt L_0 in the WF law ($\kappa_e/\sigma T = L$, σ : electrical conductivity) to calculate the electronic thermal conductivity.

Figure 2c plots the measured total thermal conductivity (κ_t) as well as the derived electron and phonon contributions (κ_e and κ_{ph}). An important feature in κ_t is that it exhibits two local maxima at 145 K and 59 K, which correlates perfectly with the onset temperature of the two CDWs. More interesting observations come from κ_e and κ_{ph} . At the two T_{CDW} , κ_e displays abrupt drops, in agreement with the observed reduction in κ_t . It has been shown that the first CDW phase transition removes roughly half of the total charge carriers ($n = 3.8 \times 10^{21}$ cm⁻³ at 300 K), and the second leaves only a small part of the Fermi surface ungapped with $n = 6 \times 10^{18}$ cm⁻³. As such, the variation in κ_e is a direct result of conduction electron condensation due to CDWs.

More attractively, κ_{ph} presents an unusual temperature dependence with two distinct signatures corresponding to the two CDWs. As shown in Figure 2c, κ_{ph} displays a trend of $T^{-0.51}$ in the high temperature range. However, with the onset of the first CDW, the normal concave-up curve converts into a concave-down trend; and as the temperature drops to 59 K, a sharp peak appears. The coincidence of the anomalies in κ_e and κ_{ph} at both CDW transitions indicates that the abnormal peaks in κ_{ph} near T_{CDW1} and T_{CDW2} are indeed due to changes in the concentration of free electrons. Importantly, κ_e and κ_{ph} demonstrate exact opposite temperature dependence in the two CDW regimes, which strongly suggests that the abnormal trend in κ_{ph} is due to e-ph scattering. It is important to note that while the error bar from the measurement uncertainty is comparable to the measured total thermal conductivity anomaly at T_{CDW} , it will not affect our conclusion that the distinct signatures in lattice thermal conductivity are due to e-ph scattering. This is because the ~11% uncertainty primarily arises from errors in the nanowire dimensions as a systematic error for all κ_t , κ_e and κ_{ph} . The random errors that could cast doubt on the anomalous peaks is really small with a value of ~2%, much less than the magnitude of the anomalous peaks (Section VI Supporting Information).

For a normal metallic nanowire, κ_e can be estimated by $\kappa_e = \frac{1}{3}C_ev_Fl_e$, where C_e , v_F , and l_e denote electron specific heat, group velocity (Fermi velocity), and mean free path (mfp), respectively. In the low temperature regime, boundary scattering leads to a constant l_e , and κ_e follows the temperature dependence of C_e as $\kappa_e \propto T$. At high temperatures, e-ph interactions dominate electron scattering with $l_e \propto I/T$ as temperature rises above the Debye temperature (Θ_D), which yields a nearly constant κ_e .²⁸ A smooth transition connects these two limits. For NbSe₃, Θ_D is about 200 K (Section VIII Supporting Information), and the obtained κ_e is indeed approximately constant for T > 145 K, which also explains the flatter temperature dependence of κ_t ($T^{0.27}$) compared to κ_{ph} in high temperature regime. However, this NbSe₃ nanowire demonstrates a non-monotonic κ_e in the regime of the first CDW and a much larger slope in the regime of the second CDW, which can only be explained by the electron condensation during the CDW phase transitions.

An important trait of NbSe₃ is that its κ_e and κ_{ph} are comparable and as a result, distinct signatures in κ_{ph} appears due to e-ph coupling. Different from NbSe₃, for CDW material 1*T*-TaS₂, even though the measured κ_t displays a sharp drop at the onset of CDW, the reduction is fully attributed to κ_e with marginal change in κ_{ph} .²⁹ Moreover, for some other CDW materials, such as $K_{0.3}$ MoO₃ and (TaSe₄)₂I,³⁰ κ_{ph} does display abnormal peaks but they are attributed to phasons but not e-ph scattering. In this case, the CDW is driven by the conventional Peierls transition involving Fermi-surface nesting and a strong softening in the low-energy phonon spectrum (Kohn anomaly).^{3,15,16} However, recent inelastic x-ray scattering measurements on NbSe₃ show no sign of softening in phonon dispersion, and the CDWs in NbSe₃ have been attributed to charge redistribution driven by strong e-ph coupling, evidenced by a strong phonon line broadening at the location of CDW wave vector.³¹ In this case, the phonon group velocity and lattice specific heat do not vary significantly across the CDW phase transition.^{18,32,33} For example, the measured

Young's modulus E shows a very small anomaly at 145 K, and $\Delta E/E_0$, where ΔE is the difference of the measured E and the extrapolated E_0 according to the pre-transition behavior, is measured to be ~0.09%.³² Moreover, no anomaly or slope change ($\Delta E/E_0 < 0.01\%$) is detected at 59 K.³² Similar results have been observed in the specific heat measurement, where the measured anomaly, defined as $\Delta C/C_0$, is merely 3% and 1% at 145 K and 59 K, respectively.³³ Therefore, the unique temperature dependence of κ_{ph} observed in our NbSe₃ nanowires must come from the change in phonon mfp, due to changes in e-ph scattering, but not lattice specific heat variations.

For NbSe₃ nanowires with D_h less than the electron mfp, boundary scattering poses additional resistance to electron transport (Section III Supporting Information).³⁴ This is manifested in Figure 3a, where the room temperature electrical resistivity escalates as D_h reduces. Moreover, as the CDW phase transition temperatures and the presence of abnormal peaks in R(T) do not change for D_h down to 30 nm, the long-range order of CDWs are preserved in the measurement size regime.^{4,15} As shown in Figure 3b, the higher electrical resistivity corresponds to lower κ_e . The amplitude of κ_e variations during CDW phase transitions also become significantly smaller; and as D_h reduces to 36 nm, the non-monotonic trend disappears. In addition, even though the carrier concentration remains largely unchanged as manifested by the nearly overlapped Seebeck coefficients for different size nanowires (Section III Supporting Information), the enhanced phonon boundary scattering in smaller wires becomes more dominant and the distinct signatures in κ_{ph} induced by CDWs become less significant, as shown in Figure 3c. The systematic and correlated changes in σ_s , κ_e , and κ_{ph} versus D_h allow for examination of the effects of different factors though modeling.

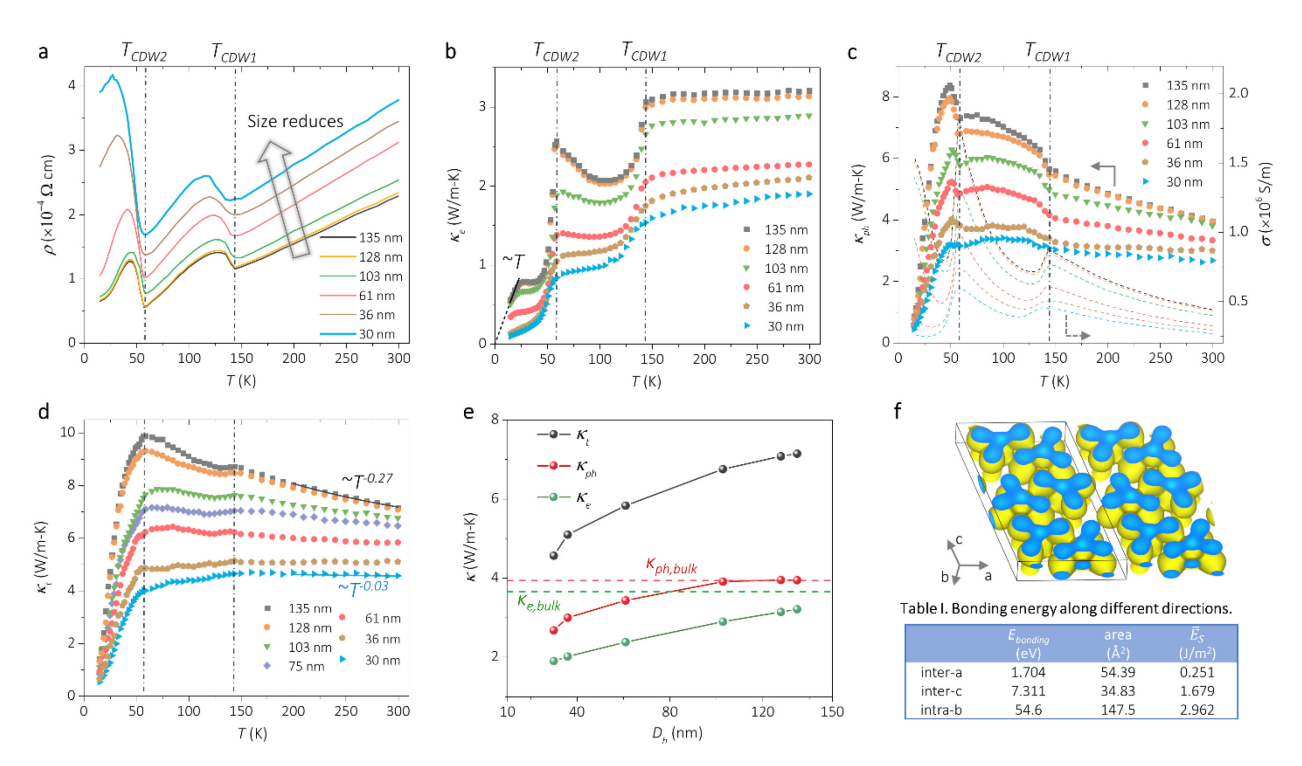


Figure 3. Size dependent thermal/electrical transport in NbSe₃ nanowires. (a-b) Measured electrical resistivity and derived electronic thermal conductivity of different size NbSe₃ nanowires in the temperature regime of 15-300 K. (c) Extracted lattice thermal conductivity (left axis), and the measured electrical conductivity of different size nanowires (right axis). (d) Measured total thermal conductivity. (e) Room temperature total thermal conductivity, electronic and lattice thermal conductivity plotted as a function of hydraulic diameter. (f) Top: simulated isosurface of electron density (0.27 e/Å^3) , and Bottom: Table I depicting the bonding energy along different crystalline directions. Here $E_{bonding}$ is the calculated total bonding energy for each crystal plane, and \overline{E}_S is the average bonding energy per unit area.

Figure 3d plots κ_t for different diameter wires and despite the anisotropic quasi-1D structure of NbSe₃, κ_t still demonstrates a clear size dependence, with the temperature dependence varies from $T^{0.03}$ to $T^{0.27}$ for T > 200 K as D_h increases. The room temperature thermal conductivity *versus* D_h is plotted in Figure 3e, which suggests that κ_{ph} saturates at $D_h = 103$ nm while κ_e keeps increasing. This observation is consistent with the common understanding that electrons have a larger mfp than phonons in metals.^{12,13} The persistent size dependence of κ_{ph} is somewhat unexpected given the quasi-1D nature of NbSe₃. However, as the calculated bonding energy shows (Table I in Figure 3f), the bonding strength along the c-direction (1.679 J/m²) is comparable to that

along the *b*-direction (2.962 J/m²) of the wire axis (Section IX Supporting Information). This rather strong inter-chain bonding leads to relatively weak phonon focusing and substantial phonon boundary scattering, which is also supported by the fact that the thermal conductivity only increases slightly with the sample length and saturates at a relatively short length of $< 6 \mu m$ (Section V Supporting Information). Note that to exclude the effects from the ballistic transport of phonons in the measured thermal conductivity, we make sure that the suspended lengths of all tested samples are larger than $6 \mu m$ to ensure a meaningful comparison between wires of different hydraulic diameters.

To further understand the effects of e-ph interactions, we combine first-principles calculations with phenomenological models. The phonon dispersion of NbSe₃ was first calculated using the derived force constants and the phonopy package (Figure S11).^{35–37} We then solve for κ_{ph} along the *b*-direction using³⁸

$$\kappa_{ph} = \frac{1}{k_B T^2 \Omega N} \sum_{j} f_0 \left(f_0 + 1 \right) \left(\hbar \omega \nu_j \right)^2 \tau_j , \qquad (1)$$

where k_B , T, Ω , N, \hbar , ω , and v_j are the Boltzmann constant, temperature, volume of unit cell, number of wave vector points, reduced Plank constant, phonon frequency and mode j dependent phonon group velocity, respectively. f_0 is the equilibrium Bose-Einstein distribution, and the mode dependent phonon relaxation time τ_j is considered using the Matthiessen's rule, taking into account of the boundary, Umklapp, defects and e-ph scattering. Particularly, the e-ph scattering lifetime $\tau_{j,e-ph}$ is calculated using Ziman's formula, $\tau_{j,e-ph}^{-1} = \frac{(m_e E_D)^2 k_B T}{2\pi \rho \hbar^4 v_j^2} \chi_{\omega}$, where m_e and ρ are the effective electron mass and mass density, respectively, and $\chi_{\omega} = \hbar \omega / k_B T$. E_D is deformation potential, which is shown to correlate with carrier density n as $E_D \propto n^{2/3}$. We note that for really small wires (<10 nm diameter), it has been predicted that the e-ph scattering rate could be higher

than the bulk value due to confinement;^{40,41} however, our wires are still in the classical size effect regime and the measured resistivity resemble the shape of the bulk resistivity, indicating that the e-ph scattering rate does not deviate significantly from the bulk value.

The modeling results for three different wires ($D_h = 135$, 61, 30 nm) are shown in Figure 4a, and the only parameter varying from wire to wire is the boundary scattering term. For the sample with $D_h = 135$ nm, the modeled κ_{ph} without considering e-ph scattering displays a trend of $T^{0.8}$, exhibiting a stronger temperature dependence compared to the measured κ_{ph} and approaches the T^{-1} behavior for bulk single crystalline materials. Moreover, extensive modeling efforts show that without considering e-ph scattering, κ_{ph} always follows the typical shape for crystalline materials with a smooth profile in the whole temperature range, no matter how we tune different scattering mechanisms. Only with the e-ph scattering term introduced, the modeled κ_{ph} can fit the experimental data well, which strongly indicates that it is indeed the e-ph scattering that leads to the distinct signatures in κ_{ph} .

To demonstrate the uniqueness of different fitting parameters, we solve for the sensitivity coefficients (S_{α}) defined as the fractional variation of κ_{ph} with respect to each fitting parameter (α) in different scattering terms, given by $S_{\alpha} = \partial \left[\ln(\kappa_{ph})\right]/\partial \left[\ln(\alpha)\right].^{42}$ Figure 4b depicts the calculated S_{α} for the boundary, Umklapp, defects, and e-ph scattering parameters as a function of temperature. Consistent with conventional understanding, the magnitude of S_{α} manifests the dominant role of boundary, defects, and Umklapp scatterings in the low, peak thermal conductivity, and high temperature regimes. Importantly, S_{α} for the e-ph scattering term shows two anomalous jumps at the onset of the CDW phase transition temperatures, indicating its dominant role for the abnormal peaks observed in κ_{ph} . Comparison of the mode dependent scattering rates derived from the best fitting parameters for the 135 nm NbSe₃ nanowire at 59 K (Figure S13) further confirms

the above conclusion. We note that the extracted e-ph scattering rate is comparable to or a little higher than those for heavily doped Si⁸ and normal metals.^{12,13}

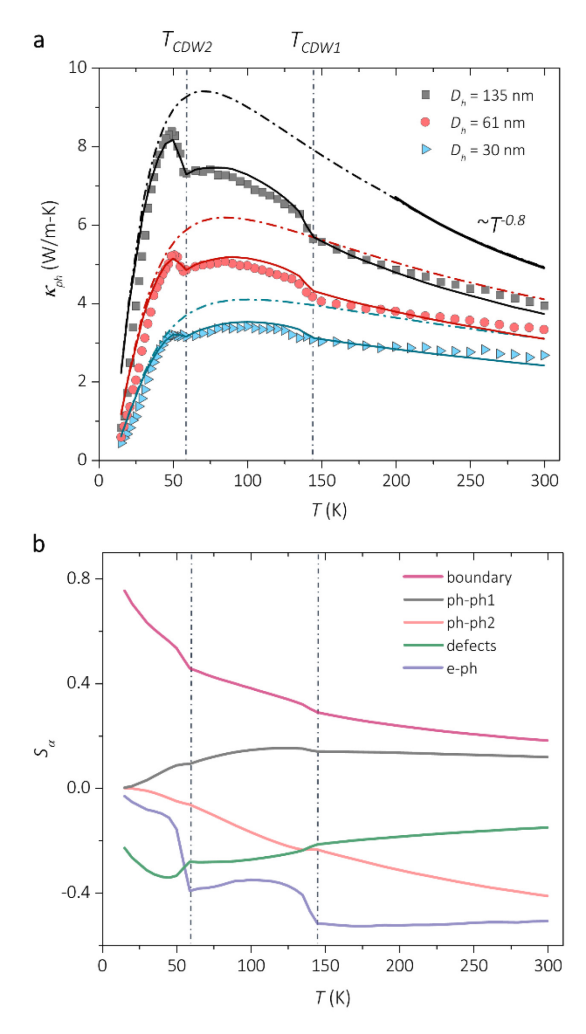


Figure 4. Modeling results showing the critical role of e-ph scattering. (a) Comparison between fitted and measured lattice thermal conductivity for three NbSe₃ nanowires with D_h of 135, 61 and 30 nm, where the dashed and solid lines show the modeling result without and with taking the e-ph scattering into consideration, respectively. (b) Sensitivity analysis for different scattering mechanisms, where anomalous jumps corresponding to the two CDW phase transitions could be observed in S_{e-ph} . Here, ph-ph1 and ph-ph2 are the two fitting parameters for the Umklapp scattering mechanism.

Moreover, Fig. 4b indicates that above 150 K, the sensitivity coefficients for the e-ph scattering and defect scattering demonstrate similar temperature dependence, which means that in this regime, one could fit the measured lattice thermal conductivity by tuning either of the two

fitting parameters. This is probably the reason why even though the effects of e-ph scattering are usually neglected in modeling the lattice thermal conductivity of heavily doped semiconductors, as pointed out by Liao et al., a fairly good fitting can still be obtained through adjusting the fitting parameter for defect scattering. The distinct signatures in the lattice thermal conductivity of NbSe3 nanowires disclosed here, however, clearly indicate the importance of e-ph interactions in determining the lattice thermal conductivity and help to understand its contributions quantitatively.

In summary, systematic studies on transport properties of NbSe₃ nanowires disclose distinct signatures of e-ph scattering on lattice thermal conductivity due to CDW phase transitions, which provides answers to long-standing, fundamental questions of whether and how e-ph interactions affect phonon transport. Given the ubiquitous nature of e-ph coupling in heavily-doped semiconductors and metals, this discovery urges re-examination of thermal transport processes in microelectronic, photovoltaic and optoelectronic devices, which could improve device design and performance.

METHODS

NbSe₃ Nanowires Sample Preparation. Multi-millimeter long ribbon-like NbSe₃ crystals were grown by chemical vapor transport (CVT) method (Section I Supporting Information). We obtained individual nanowire samples using a liquid exfoliation method. To do this, bulk NbSe₃ single crystal whiskers was immersed in reagent alcohol and sonicated for 3 hours, which resulted in a suspension of nanowires with various cross-sectional sizes. As shown in the high resolution transmission electron microscopy (HRTEM) image (Figure S1), NbSe₃ nanowires obtained by this method demonstrates well-aligned molecular chains of single crystalline nature. We finally drop-casted the suspension mixture onto the surface of a piece of polydimethylsiloxane (PDMS), and transferred individual nanowire samples to our suspended microdevice with a custom-built micromanipulator for subsequent thermal and electrical properties measurement.

Electrical and Thermal Transport Properties Measurements. We conducted the electrical and thermal measurements in a cryostat (Janis CCS-400/204) operated under high vacuum (<1×10⁻⁶ mbar) with a dual radiation shield configuration. ^{19,23,43} Before thermal conductivity measurements at each designated temperature point, we measured the electrical resistance of NbSe₃ nanowire samples using the four-probe method (Section III Supporting Information). EBID of Pt/C composite was performed at the contacts between the nanowire and Pt electrodes using a dual beam system (FIB/SEM, FEI Helios NanoLab G3, Figure 1b) to establish good electrical contacts and minimize the contact thermal resistance. To exclude the effects from CDW sliding, we make sure the applied electric field to be much smaller than the depinning threshold electrical field, ¹⁵ and the obtained *I-V* curve maintain a linear shape at all temperature points.

For thermal conductivity measurements, a Wheatstone bridge scheme was applied at the sensing side of the measurement device to improve measurement sensitivity.²⁰ The background

thermal conductance between the suspended membranes was measured separately and subtracted from the measured thermal conductance of the sample.²³ To evaluate the thermal and electrical conductivity, we obtained the exact cross-sectional area of each tested sample by cutting open the cross-section using a high ion current.²² During the thermal measurements, we also measured Seebeck coefficient for each sample by monitoring the temperature difference of the two suspended membranes and the induced voltage difference (SR560) across the two inner electrodes (Section III Supporting Information).

Author Contributions

L.Y. conducted thermal/electrical property measurements; Y.T., L.Y., C.L., and Y.C. performed theoretical modeling; J.L. and Z.M. synthesized the materials; M.A. and T.X. performed TEM studies; D.L. supervised the project; L.Y. and D.L. analyzed the results with input from all authors.

Conflict of Interest

The authors declare no competing financial interests.

Acknowledgements

The authors thank the financial support from the U.S. National Science foundation (DMR-1308550, DMR-1308509, CBET-1403456, DMR-1532107, CBET-1805924), and from NEEC (Grant# N00174-16-C-0008). Work at Tulane University (material synthesis) was supported by the US Department of Energy under grant DE-S14208. C.L. acknowledges financial support from the China Scholarship Council (CSC 201606090029).

ASSOCIATED CONTENT

Supporting Information

The Supporting Information is available free of charge on the ACS Publication website *via* the Internet at http://pubs.acs.org.

Additional information for sample preparation and cross-section characterization; electrical resistance and Seebeck coefficient measurements; contact thermal resistance characterization, length dependent thermal conductivity measurement, and experimental uncertainty; Lorenz number calculation; Debye temperature calculation; bonding energy calculation; additional information on the modeling to extract the contribution of e-ph scattering.

References

- (1) Lanzara, A.; Bogdanov, P. V.; Zhou, X. J.; Kellar, S. A.; Feng, D. L.; Lu, E. D.; Yoshida, T.; Eisaki, H.; Fujimori, A.; Kishio, K.; Shimoyama, J.-I.; Noda, T.; Uchida, S.; Hussain, Z.; Shen, Z.-X. Evidence for Ubiquitous Strong Electron–phonon Coupling in High-Temperature Superconductors. *Nature* 2001, 412 (6846), 510–514.
- (2) Herring, C. Theory of the Thermoelectric Power of Semiconductors. *Phys. Rev.* **1954**, *96* (5), 1163–1187.
- (3) Peierls, R. Quantum Theory of Solids; Oxford Univ Press, New York, 1955.
- (4) Xi, X.; Zhao, L.; Wang, Z.; Berger, H.; Forró, L.; Shan, J.; Mak, K. F. Strongly Enhanced Charge-Density-Wave Order in Monolayer NbSe2. *Nat. Nanotechnol.* **2015**, *10* (9), 765–769.
- (5) Ziman, J. The Theory of Transport Phenomena in Solids; Clarendon Press, Oxford, 1960.
- (6) Lundstrom, M. Fundamentals of Carrier Transport; Cambridge University Press, Cambridge, England, 2009.
- (7) Butler, W. H.; Williams, R. K. Electron-Phonon Interaction and Lattice Thermal Conductivity. *Phys. Rev. B* **1978**, *18* (12), 6483–6494.
- (8) Liao, B.; Qiu, B.; Zhou, J.; Huberman, S.; Esfarjani, K.; Chen, G. Significant Reduction of Lattice Thermal Conductivity by the Electron-Phonon Interaction in Silicon with High Carrier Concentrations: A First-Principles Study. *Phys. Rev. Lett.* 2015, 114 (11), 115901.
- (9) Morelli, D. T.; Heremans, J. P.; Beetz, C. P.; Yoo, W. S.; Matsunami, H. Phonon-Electron Scattering in Single Crystal Silicon Carbide. *Appl. Phys. Lett.* **1993**, *63* (23), 3143–3145.
- (10) Holland, M. G. Phonon Scattering in Semiconductors From Thermal Conductivity Studies. *Phys. Rev.* **1964**, *134* (2A), A471–A480.

- (11) Liao, B.; Maznev, A. A.; Nelson, K. A.; Chen, G. Photo-Excited Charge Carriers Suppress Sub-Terahertz Phonon Mode in Silicon at Room Temperature. *Nat. Commun.* **2016**, *7*, 13174.
- Wang, Y.; Lu, Z.; Ruan, X. First Principles Calculation of Lattice Thermal Conductivity of Metals Considering Phonon-Phonon and Phonon-Electron Scattering. *J. Appl. Phys.* 2016, 119 (22), 225109.
- (13) Jain, A.; McGaughey, A. J. H. Thermal Transport by Phonons and Electrons in Aluminum, Silver, and Gold from First Principles. *Phys. Rev. B* **2016**, *93* (8), 081206.
- (14) Zheng, Q.; Mei, A. B.; Tuteja, M.; Sangiovanni, D. G.; Hultman, L.; Petrov, I.; Greene, J. E.; Cahill, D. G. Phonon and Electron Contributions to the Thermal Conductivity of VNx Epitaxial Layers. *Phys. Rev. Mater.* 2017, *1* (6), 065002.
- (15) Grüner, G. The Dynamics of Charge-Density Waves. *Rev. Mod. Phys.* **1988**, *60* (4), 1129–1181.
- (16) Zhu, X.; Cao, Y.; Zhang, J.; Plummer, E. W.; Guo, J. Classification of Charge Density Waves Based on Their Nature. *Proc. Natl. Acad. Sci.* **2015**, *112* (8), 2367–2371.
- (17) Van Smaalen, S.; De Boer, J. L.; Meetsma, A.; Graafsma, H.; Sheu, H. S.; Darovskikh,
 A.; Coppens, P.; Levy, F. Determination of the Structural Distortions Corresponding to
 the Q1- and Q2-Type Modulations in Niobium Triselenide NbSe3. *Phys. Rev. B* 1992, 45
 (6), 3103–3106.
- (18) Hodeau, J. L.; Marezio, M.; Roucau, C.; Ayroles, R.; Meerschaut, A.; Rouxel, J.;
 Monceau, P. Charge-Density Waves in NbSe3 at 145K: Crystal Structures and Electron
 Diffraction Studies. J. Phys. C Solid State Phys. 1978, 11, 4117–4130.
- (19) Shi, L.; Li, D.; Yu, C.; Jang, W.; Kim, D.; Yao, Z.; Kim, P.; Majumdar, A. Measuring

- Thermal and Thermoelectric Properties of One-Dimensional Nanostructures Using a Microfabricated Device. *J. Heat Transfer* **2003**, *125* (5), 881.
- (20) Wingert, M. C.; Chen, Z. C. Y.; Kwon, S.; Xiang, J.; Chen, R. Ultra-Sensitive Thermal Conductance Measurement of One-Dimensional Nanostructures Enhanced by Differential Bridge. *Rev. Sci. Instrum.* **2012**, *83* (2), 114901.
- (21) Zhang, Q.; Cui, Z.; Wei, Z.; Chang, S. Y.; Yang, L.; Zhao, Y.; Yang, Y.; Guan, Z.; Jiang, Y.; Fowlkes, J.; Yang, J.; Xu, D.; Chen, Y.; Xu, T. T.; Li, D. Defect Facilitated Phonon Transport through Kinks in Boron Carbide Nanowires. *Nano Lett.* 2017, 17 (6), 3550–3555.
- (22) Zhang, Q.; Liu, C.; Liu, X.; Liu, J.; Cui, Z.; Zhang, Y.; Yang, L.; Zhao, Y.; Xu, T. T.;
 Chen, Y.; Wei, J.; Mao, Z.; Li, D. Thermal Transport in Quasi-1D van Der Waals Crystal
 Ta2Pd3Se8 Nanowires: Size and Length Dependence. ACS Nano 2018, 12 (3), 2634–
 2642.
- (23) Yang, L.; Yang, Y.; Zhang, Q.; Zhang, Y.; Jiang, Y.; Guan, Z.; Gerboth, M.; Yang, J.; Chen, Y.; Walker, D. G.; Xu, T.T.; Li, D. Thermal Conductivity of Individual Silicon Nanoribbons. *Nanoscale* **2016**, *8* (41), 17895–17901.
- (24) Slot, E.; van der Zant, H. S. J.; O'neill, K.; Thorne, R. E. Crossover from Two-Dimensional to One-Dimensional Collective Pinning in NbSe3. *Phys. Rev. B - Condens. Matter Mater. Phys.* **2004**, *69* (7), 073105.
- (25) Chaikin, P. M.; Fuller, W. W.; Lacoe, R.; Kwak, J. F.; Greene, R. L.; Eckert, J. C.; Ong, N. P. Thermopower of Doped and Damaged NbSe3. *Solid State Commun.* 1981, 39 (4), 553–557.
- (26) Kim, H. S.; Gibbs, Z. M.; Tang, Y.; Wang, H.; Snyder, G. J. Characterization of Lorenz

- Number with Seebeck Coefficient Measurement. APL Mater. 2015, 3 (4), 041506.
- (27) Adelman, T. L.; Zaitsev-Zotov, S. V.; Thorne, R. E. Field-Effect Modulation of Charge-Density-Wave Transport in NbSe3 and TaS3. *Phys. Rev. Lett.* **1995**, *74* (26), 5264–5267.
- (28) Kim, T. Y.; Park, C.-H.; Marzari, N. The Electronic Thermal Conductivity of Graphene. Nano Lett. 2016, 16 (4), 2439–2443.
- (29) Núñez-Regueiro, M.; Lopez-Castillo, J.; Ayache, C. Thermal Conductivity of 1T-TaS2 and 2H-TaSe2. *Phys. Rev. Lett.* **1985**, *55* (18), 1931–1934.
- (30) Kwok, R. S.; Brown, S. E. Thermal Conductivity of the Charge-Density-Wave Systems K0.3MoO3 and (TaSe4)2I near the Peierls Transition. *Phys. Rev. Lett.* **1989**, *63* (8), 895–898.
- (31) Requardt, H.; Lorenzo, J. E.; Monceau, P.; Currat, R.; Krisch, M. Dynamics in the Charge-Density-Wave System NbSe3 Using Inelastic x-Ray Scattering with MeV Energy Resolution. *Phys. Rev. B* **2002**, *66* (21), 214303.
- (32) Brill, J. W.; Ong, N. P. Young's Modulus of NbSe3. *Solid State Commun.* **1977**, *25* (12), 1075—1078.
- (33) Tomić, S.; Biljakovic, K.; Djurek, D.; Cooper, J. R.; Monceau, P.; Meerschaut, A. Calorimetric Study of the Phase Transitions in Niobium Triselenide NbSe3. *Solid State Commun.* **1981**, *38* (2), 109–112.
- (34) McCarten, J.; Maher, M.; Adelman, T. L.; Thorne., R. E. Size Effects and Charge-Density-Wave Pinning in NbSe3. *Phys. Rev. Lett.* **1989**, *63* (26), 2841–2844.
- (35) Kresse, G.; Joubert, D. From Ultrasoft Pseudopotentials to the Projector Augmented-Wave Method. *Phys. Rev. B* **1999**, *59* (3), 1758–1775.
- (36) Gonze, X.; Lee, C. Dynamical Matrices, Born Effective Charges, Dielectric Permittivity

- Tensors, and Interatomic Force Constants from Density-Functional Perturbation Theory. *Phys. Rev. B* **1997**, *55* (16), 10355–10368.
- (37) Togo, A.; Oba, F.; Tanaka, I. First-Principles Calculations of the Ferroelastic Transition between Rutile-Type and CaCl2-Type SiO2 at High Pressures. *Phys. Rev. B* **2008**, *78* (13), 134106.
- (38) Li, W.; Carrete, J.; A. Katcho, N.; Mingo, N. ShengBTE: A Solver of the Boltzmann Transport Equation for Phonons. *Comput. Phys. Commun.* **2014**, *185* (6), 1747–1758.
- (39) Asheghi, M.; Kurabayashi, K.; Kasnavi, R.; Goodson, K. E. Thermal Conduction in Doped Single-Crystal Silicon Films. *J. Appl. Phys.* **2002**, *91* (8), 5079–5088.
- (40) Arbouet, A.; Voisin, C.; Christofilos, D.; Langot, P.; Fatti, N. Del; Vallée, F.; Lermé, J.;
 Celep, G.; Cottancin, E.; Gaudry, M.; Pellarin, M.; Broyer, M.; Maillard, M.; Pileni, M.P.;
 Treguer, M. Electron-Phonon Scattering in Metal Clusters. *Phys. Rev. Lett.* **2003**, *90* (17),
 177401.
- (41) Ramayya, E. B.; Vasileska, D.; Goodnick, S. M.; Knezevic, I. Electron Transport in Silicon Nanowires: The Role of Acoustic Phonon Confinement and Surface Roughness Scattering. *J. Appl. Phys.* **2008**, *104* (6), 063711.
- (42) Koh, Y. K.; Singer, S. L.; Kim, W.; Zide, J. M. O.; Lu, H.; Cahill, D. G.; Majumdar, A.; Gossard, A. C. Comparison of the 3ω Method and Time-Domain Thermoreflectance for Measurements of the Cross-Plane Thermal Conductivity of Epitaxial Semiconductors. *J. Appl. Phys.* 2009, 105 (5), 054303.
- (43) Moore, A. L.; Shi, L. On Errors in Thermal Conductivity Measurements of Suspended and Supported Nanowires Using Micro-Thermometer Devices from Low to High Temperatures. *Meas. Sci. Technol.* 2010, 22 (1), 015103.

TOC:

